A digital image correlation based methodology to characterize formability in tube forming

Valentino AM Cristino[1], Joao P Magrinho[2], Gabriel Centeno[3],
Maria Beatriz Silva[2] and Paulo AF Martins[2] (iD)

Abstract
This article describes a methodology to characterize the failure limits by necking and fracture, and to determine the critical value of ductile damage in tube forming. The methodology makes use of digital image correlation, thickness measurements and force–displacement evolutions to obtain the strain loading paths and the strain values at the onsets of failure by necking and fracture. The onset of failure by necking is determined by a new technique that combines the strain and force–displacement evolutions whereas the fracture strains at the cracked regions of the tubes are obtained by a similar technique utilized by the authors in sheet metal forming. Transformation of the strain loading paths from principal strain space into the space of effective strain versus stress-triaxiality allows determining the critical experimental value of ductile damage at the onset of failure by necking. The methodology is applied to tube expansion with circular, elliptical and square cross-section punches and results confirm its importance and helpfulness for researchers and engineers involved in the development and optimization of industrial tube forming processes.

Introduction

Digital image correlation (DIC) is a full-field optical technology that allows determining the contour and displacements of a specimen by tracing and comparing digital photographs at different instants of deformation.[1] In recent years, the utilization of DIC became increasingly popular in sheet metal forming because it permits automatic evaluation of strains without tedious measurement of circle grids. This is particularly useful in the experimental characterization of the formability limits,[2,3] with the additional advantage of avoiding human intervention, which often leads to measurement errors.

The application of DIC in bulk metal forming has been limited to the determination of stress–strain curves.[4] However, recent developments by the authors showed that combination of DIC and force–displacement measurements can be successfully utilized to obtain the experimental strain loading paths up to fracture in bulk formability tests performed with cylindrical, shear, tapered and flanged specimens.[5]

The application of DIC in tube forming has also been limited. Among the few works available in

literature, it is worth mentioning the determination of the stress–strain curves[6,7] and of the anisotropic yield functions in tubular materials,[7] and the characterization of the axial crushing of tubes.[7,8] The investigation on the failure of tubes with machined grooves subjected to combined tension and torsion by Scales et al.[9] is the only publication, as far as authors are aware, that describes the utilization of DIC to determine the failure strains in tube forming. In particular, the work associates failure strains with the corresponding values of stress-triaxiality in order to obtain the necking failure locus.

[1]Department of Electromechanical Engineering, University of Macau, Taipa, China
[2]IDMEC, Instituto Superior Tecnico, Universidade de Lisboa, Lisboa, Portugal
[3]Department of Mechanical and Manufacturing Engineering, University of Seville, Seville, Spain

Corresponding author:
Paulo AF Martins, IDMEC, Instituto Superior Tecnico, Universidade de Lisboa, Av. Rovisco Pais, Lisboa 1049-001, Portugal.
Email: pmartins@tecnico.ulisboa.pt

Under these circumstances, and similar to what the authors did in bulk forming,[5] it is the intention of this article to present a new methodology to characterize formability in tube forming. The article explains how in-plane strains obtained by DIC, gauge length strains obtained from thickness measurements after cracking and force–displacement evolutions acquired from transducers can be combined to determine the strain loading paths, the strain values at the onsets of failure by necking and fracture and the critical experimental values of ductile damage in tube forming.

The methodology is applied to tube expansion with circular, elliptical and square cross-section punches and results confirm its importance and helpfulness for researchers and engineers involved in the development and optimization of industrial tube forming processes.

Methodology

The methodology to characterize formability in tube forming is schematically depicted in Figure 1 and consists of three different stages. The special case of tube expansion with a circular cross-section punch will be utilized to illustrate its applicability throughout this section of the article.

First stage

The first stage is experimental and consists of obtaining the force–displacement evolution and the in-plane strains on the vicinity of the zone where crack is opened. The utilization of a DIC system for measuring the in-plane strains requires application of a non-uniform speckle pattern on the tube surface by first painting in white and then spraying with black droplets (Figure 1(a)).

The photographs included in Figure 1(a) show the distribution of meridional ε_ϕ and circumferential ε_θ strains at the onset of necking for tube expansion with a circular cross-section punch with the location at the vicinity of the necking where the values were obtained.

By combining the experimental strain and force–displacement evolutions, it is possible to determine the instant of time corresponding to the onset of failure by necking (Figure 1(b)). This is accomplished by identifying the punch displacement after which the evolution of force drops and the evolutions of meridional strain ε_ϕ, and circumferential strain ε_θ remain constant. The strain pairs at the onset of failure by necking are plotted as $(\varepsilon_\theta^n, \varepsilon_\phi^n)$ in Figure 1(b).

The first stage of the proposed methodology ends by merging the evolutions of meridional ε_ϕ and circumferential ε_θ strains into the strain loading path and plotting in the principal strain space (Figure 1(c)).

Second stage

The second stage consists on the transformation of the experimental strain loading path from principal strain space (Figure 1(c)) to the space of effective strain versus stress-triaxiality (Figure 1(d)). This is carried out analytically by assuming tube expansion to occur under plane stress deformation conditions ($\sigma_t = 0$) in the thickness direction, loading to be proportional and material to be isotropic.

Under these simplifying assumptions, the effective stress $\bar{\sigma}$ and the increment of effective strain $d\bar{\varepsilon}$ are expressed as follows

$$\bar{\sigma} = \sqrt{\sigma_\theta^2 + \sigma_\phi^2 - \sigma_\theta \sigma_\phi}$$
$$d\bar{\varepsilon} = \frac{2}{\sqrt{3}} \sqrt{d\varepsilon_\theta^2 + d\varepsilon_\phi^2 + d\varepsilon_\theta d\varepsilon_\phi} \tag{1}$$

Then, by applying the Levy–Mises constitutive equations, it is possible to write the effective strain $\bar{\varepsilon}$ and stress-triaxiality $\sigma_m/\bar{\sigma}$ as a function of the slope $\beta = d\varepsilon_\phi/d\varepsilon_\theta$ of the strain loading path as follows

$$\bar{\varepsilon} = \frac{2}{\sqrt{3}} \sqrt{1 + \beta + \beta^2}\, \varepsilon_\theta$$
$$\frac{\sigma_m}{\bar{\sigma}} = \frac{(1 + \beta)}{\sqrt{3}\sqrt{1 + \beta + \beta^2}} \tag{2}$$

Finally, by combining the two above equations, one obtains the following relation between the effective strain $\bar{\varepsilon}$ and the stress-triaxiality $\sigma_m/\bar{\sigma}$ that allows transforming the strain loading paths from principal strain space to the space of effective strain versus stress-triaxiality

$$\bar{\varepsilon} = \frac{2}{3}(1 + \beta)\varepsilon_\theta \left(\frac{\sigma_m}{\bar{\sigma}}\right)^{-1} = \frac{2}{3}\left(\varepsilon_\theta + \varepsilon_\phi\right)\left(\frac{\sigma_m}{\bar{\sigma}}\right)^{-1} \tag{3}$$

In the above equation, ε_θ and ε_ϕ are the circumferential and meridional in-plane strain measurements obtained by DIC.

The space of effective strain versus stress-triaxiality also allows determining the critical experimental value of ductile damage at the onset of failure by necking D_{crit}^n

$$D_{crit}^n = \int_0^{\bar{\varepsilon}^n} \frac{\sigma_m}{\bar{\sigma}} d\bar{\varepsilon} \tag{4}$$

This can be easily done by calculating the area of the grey coloured region of Figure 1(d).

The reason for choosing the void-growth damage-based criterion (4) directly related to the work of McClintock[10] is because cracks open by tension (mode I of fracture mechanics) in tube expansion, as will be seen in the section 'Results and discussion'.

Third stage

The third and final stage of the proposed methodology is aimed at distinguishing between failure strains at the onset of necking and failure strains at the onset of fracture. The former are obtained by means of the
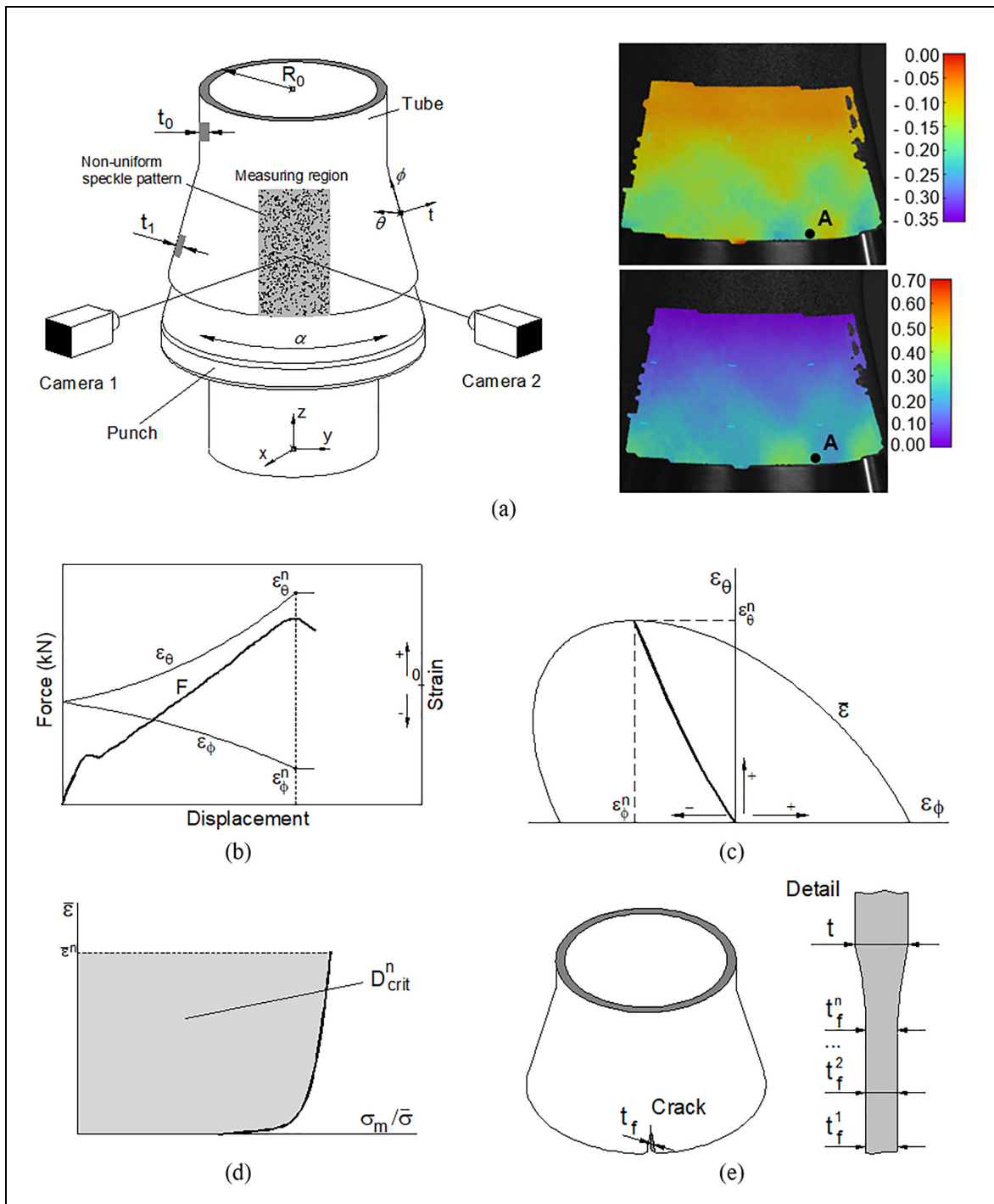
Figure 1. Graphical summary of the proposed methodology to characterize the formability limits in tube forming: (a) Schematic representation of the selected tube expansion process showing the global (x, y, z) and local (t, θ, ϕ) coordinates, the main variables and notation, the two cameras of the DIC system, the distribution of meridional ε_ϕ and circumferential ε_θ strains at the onset of failure by necking and the locations from where strains were obtained in the DIC images; (b) typical evolutions of the in-plane strains and force with displacement during tube expansion; (c) typical strain loading path, strain pairs and effective strain at the onset of failure by necking in principal strain space; (d) typical evolution of the effective strain versus stress-triaxiality derived from (c) with representation of the area corresponding to the critical ductile damage at the onset of failure by necking D_{crit}^n; and (e) schematic representation of the locations for measuring the tube thickness t_f along the crack.

experimental procedure described in the first stage whereas the latter, also known as the 'gauge length' strains, are obtained from individual measurements of the tube wall thickness along the crack with an optical microscope with a precision of ± 0.001 mm. The procedure is schematically shown in Figure 1(e) and the thickness strains at fracture ε_t^f are determined by

$$\varepsilon_t^f = \ln\frac{t_f}{t_0} \tag{5}$$

where t_0 is the initial tube wall thickness and t_f is the average tube wall thicknesses at fracture.

The meridional and circumferential strains at fracture are obtained assuming that localization gives rise to plane-strain deformation in the meridional direction ϕ after necking

$$\varepsilon_\phi^f = \varepsilon_\phi^n$$
$$\varepsilon_\theta^f = -\left(\varepsilon_t^f + \varepsilon_\phi^f\right) \tag{6}$$

The above-described procedure to determine the gauge length strains at fracture is an extension to tube forming of an earlier procedure developed by the authors to sheet metal forming.[11]

Experimentation

Stress–strain curve

The experimental work was carried out in aluminium AA6063T6 tubes with an outside radius $R_0 = 20\,\text{mm}$ and a wall thickness $t_0 = 2\,\text{mm}$. The stress–strain curve of the material was determined by means of tensile and stack compression tests in specimens that were machined out from the supplied tubes. The tensile test specimens were prepared in accordance to the ASTM E8/E8M standard[12] and the stack compression test specimens were performed in multi-layer cylinder specimens that were assembled by piling up circular discs with 10 mm diameter and 2 mm thickness.

The tests were carried out at room temperature under quasi-static loading conditions and were carried out in a hydraulic testing machine with a constant moving cross-head speed equal to 5 mm/min. The stress–strain curve that resulted from merging the experimental data from the two different types of tests is shown in Figure 2.

For additional information and details regarding the determination of the stress–strain curve of aluminium AA6063T6, please refer to a previous work of the authors.[13]

Tube expansion tests

The proposed methodology was applied to characterize formability in tube expansion with circular, elliptical and square cross-section punches. The tests were performed at room temperature on the hydraulic testing machine that had been utilized in the mechanical characterization of the aluminium AA6063T6 tubes. The tubes were lubricated with molybdenum disulphide grease (MoS_2) before being expanded and the geometry of the punches is given in Table 1.

Strain measurements on the vicinity of the zones where cracks are opened were performed with a DIC system from Dantec Dynamics (model Q-400 3D)
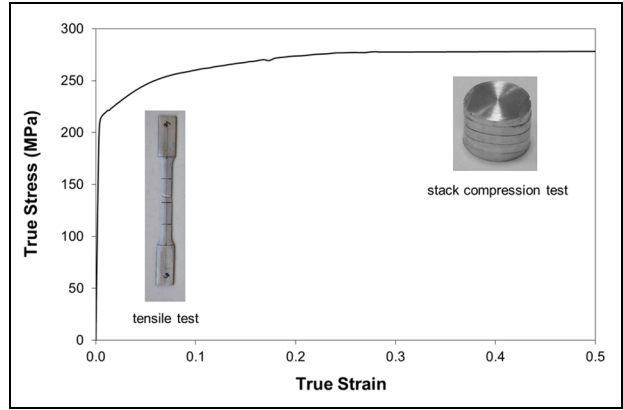
Figure 2. True stress–true strain curve of the aluminium AA6063T6 tubes obtained from tensile and stack compression tests.[12] The photograph shows two different specimens.

Table 1. Geometries of the punches utilized in the tube expansion tests.

| Geometry	ψ (°)	R (mm)	A (mm)	B (mm)	L (mm)	R_c (mm)
Circular	15	18	–	–	–	–
Elliptical	15	18	72	36	–	–
Square	15	18	–	–	72	5

equipped with two cameras with a resolution of 6 megapixels and 50.2 mm focal lenses with an aperture of f/11. The measuring area was illuminated by a spotlight and the images were acquired with a frequency of 20 frames per second. The analysis was performed with the INSTRA 4D from Dantec Dynamics, and a facet size of 13 pixels with a grid spacing of 7 pixels was considered for the correlation algorithm.

Finite element analysis

The presentation of the new proposed methodology is supported by numerical modelling of tube expansion. The simulations were performed in the computer program i-form developed by the authors that is based on the irreducible finite element flow formulation

$$\Pi = \int_V \bar{\sigma}\,\dot{\bar{\varepsilon}}\,dV + \frac{1}{2}K\int_V \dot{\varepsilon}_v^2\,dV - \int_{S_T} T_i u_i\,dS + \int_{S_f}\left(\int_0^{|u_r|}\tau_f\,du_r\right)dS \tag{7}$$

In the above functional, $\bar{\sigma}$ is the effective stress, $\dot{\bar{\varepsilon}}$ is the effective strain rate, $\dot{\varepsilon}_V$ is the volumetric strain rate,
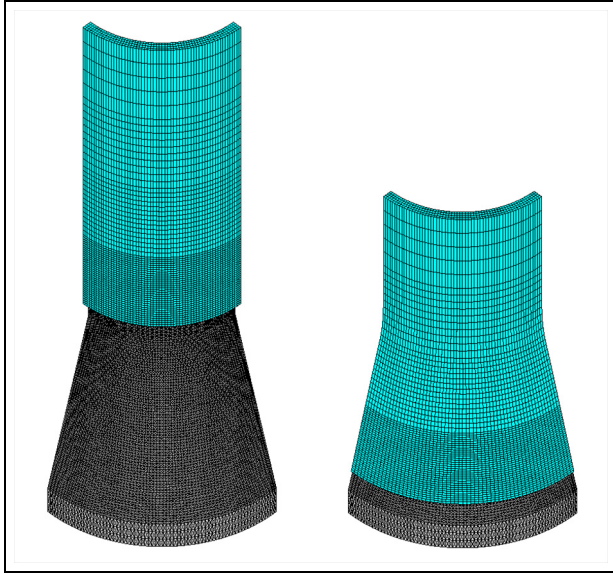
Figure 3. Initial and final computed meshes for the numerical simulation of tube expansion with a circular cross-section punch.
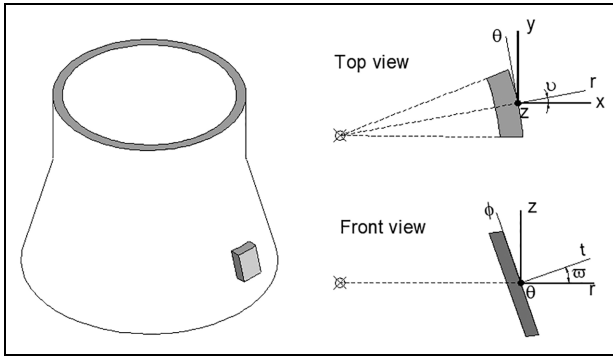
Figure 4. Schematic representation of the rotation of axis from global to local coordinates aligned with the thickness, circumferential and meridional directions of the outer surface.

K is a large positive constant imposing the material incompressibility constraint, T_i and u_i are the surface tractions and velocities on S_T, u_r and τ_f are the relative velocity and the friction shear stress (according to the law of constant friction $\tau_f = mk$) on the contact interface S_f between the tube and the punch or die, and V is the control volume limited by the surfaces S_U and S_T. Additional information and details regarding the computer implementation of the finite element flow formulation can be found elsewhere.[14]

Discretization of the tubes took advantage of symmetry boundary conditions to consider only one-quarter of the overall geometry (i.e. to reduce the tube to a 90° slice) and was carried out by a structured mesh of hexahedra with four layers across thickness. The punches and dies were modelled as rigid objects and were discretized by means of contact-friction spatial triangular elements. Different models were setup in order to simulate tube expansion with various punch geometries. Figure 3 shows the initial and final computed meshes for the tube expansion with a circular cross-section punch.

The computer program provides the strain estimates in global coordinates (x, y, z). Therefore, in order to compare these estimates with the in-plane measurements obtained by DIC, it is necessary to rotate the strain tensor ε_{ijk} into the local coordinate system (t, θ, ϕ) aligned with the thickness t, the circumferential θ and the meridional ϕ directions of a specific location on the tube surface. The rotation of the strain tensor ε_{ijk} from global to local coordinates for a specific location on the tube surface is accomplished by

$$\varepsilon_{t,\theta,\phi} = \mathbf{R}_2^T \varepsilon_{r,\theta,z} \mathbf{R}_2 = \mathbf{R}_2^T \left(\mathbf{R}_1^T \varepsilon_{x,y,z} \mathbf{R}_1 \right) \mathbf{R}_2$$

$$\mathbf{R}_1 = \begin{pmatrix} \cos\upsilon & \sin\upsilon & 0 \\ -\sin\upsilon & \cos\upsilon & 0 \\ 0 & 0 & 1 \end{pmatrix} \quad \mathbf{R}_2 = \begin{pmatrix} \cos\varpi & 0 & \sin\varpi \\ 0 & 1 & 0 \\ -\sin\varpi & 0 & \cos\varpi \end{pmatrix}$$

$$(8)$$

where $\mathbf{R}_1$ is the rotation transformation matrix about the z-axis (refer to angle υ in Figure 4) and $\mathbf{R}_2$ is the rotation transformation matrix about the θ-axis (refer to angle ϖ in Figure 4).

The simulations of tube expansion with circular, elliptical and square cross-section punches were performed through a succession of displacement increments each of one corresponding to approximately 0.1% of the initial tube height, and the overall CPU time for a typical analysis containing 20.000 hexahedral elements was approximately 5 h on a computer equipped with an Intel i7-6950X (3 GHz) processor.

Results and discussion

Displacement-based evolutions

The experimental evolutions of the force and of the in-plane strains with displacement are the starting point of the proposed methodology to characterize formability in tube forming (refer to 'Methodology' section).

Figure 5 shows such evolutions for tube expansion with circular, elliptical and square cross-section punches. The in-plane strains (ε_θ, ε_ϕ) were obtained by DIC and disclose a monotonic growth with positive (or negative) derivatives up to a local maximum (or minimum), after which the absolute values become constant. The force–displacement evolutions also disclose peak values after which the force drops. The force peaks are aligned with the in-plane strain peaks and the subsequent drop in force is caused by the sudden relief of stresses at necking and subsequent cracking.

The above observation allows one to determine the onset of failure by necking in tube forming from the identification of the amount of displacement (or the instant of time) when the forces and the strains reach peak values (refer to the dashed vertical lines in Figure 5(a)–(c)). This is a rather straightforward procedure when compared with the identification and interpolation methods that are commonly utilized in sheet metal forming[15] to identify necking and obtain the corresponding failure strains.
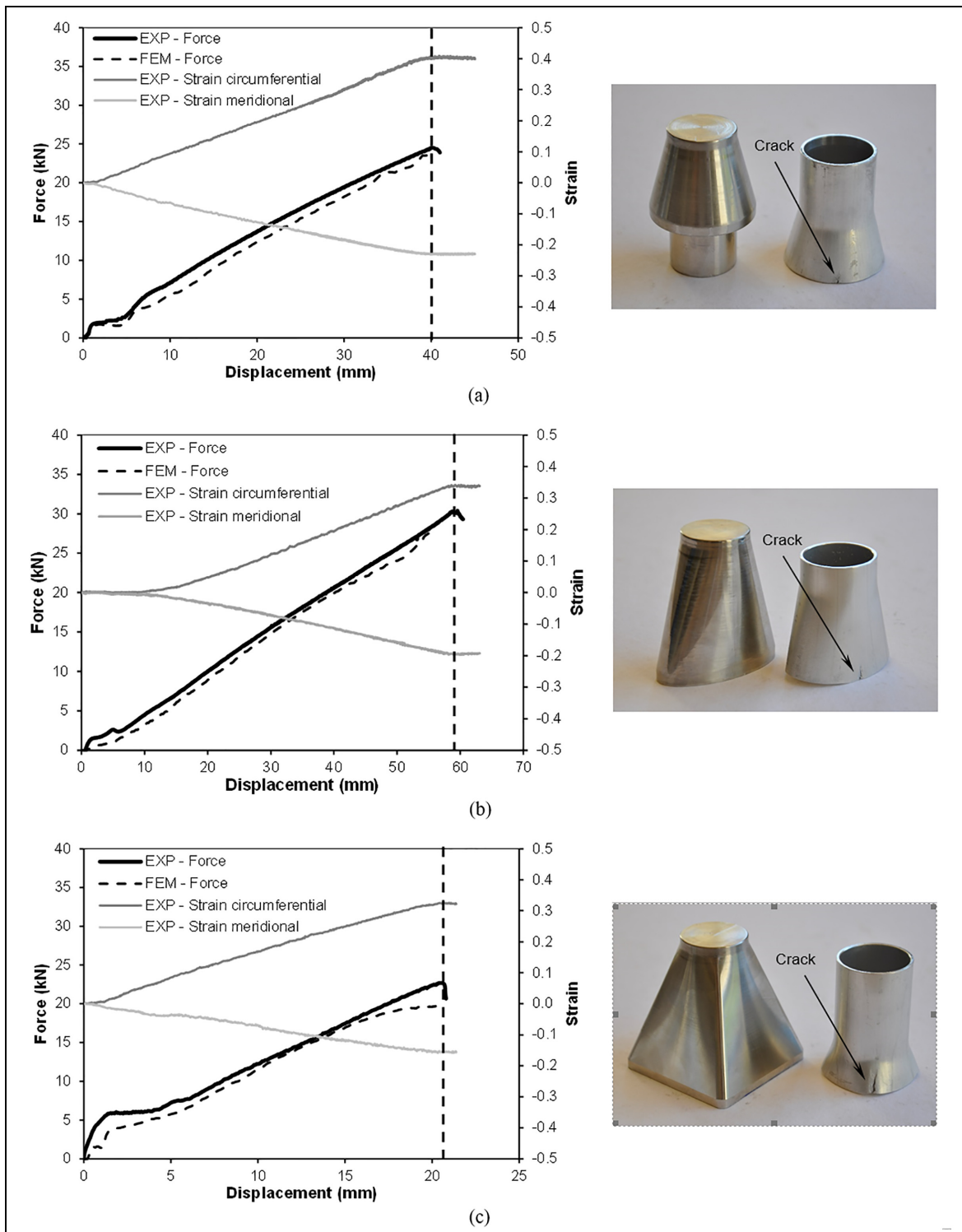
Figure 5. Experimental force–displacement and strain–displacement evolutions for tube expansion with (a) circular, (b) elliptical and (c) square cross-section punches with photographs of the punches and tubes at the end of the expansion tests. The dashed evolutions of the force with displacement were obtained by finite element analysis.

In addition to what was said above, it is worth mentioning that the overall procedure proposed by the authors is the only one applicable to tube forming because all the attempts made by the authors to extend the identification and interpolation methods of sheet metal forming to tube forming revealed ineffective. In

particular, the time-dependent methodology could not be applied due to the oscillations of the major strain rate that made identification of the maximum value extremely unreliable.

Necking is triggered on the minor axis of the elliptical cross section of the tubes and on the corner radius
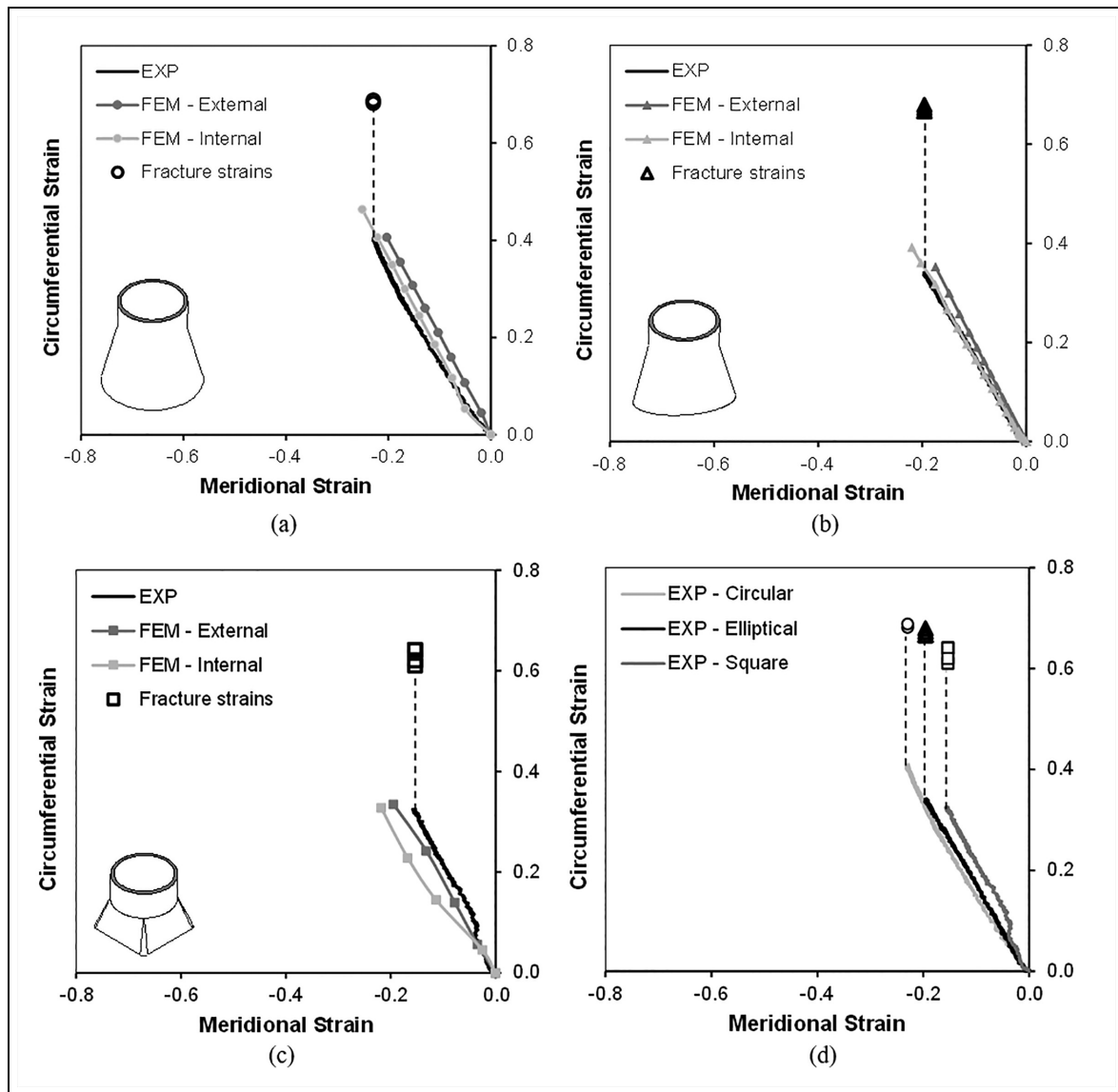
Figure 6. Experimental and finite element computed strain loading paths in principal strain space for tube expansions with (a) circular, (b) elliptical and (c) square cross-section punches. The resume of the three experimental loading paths is shown in (d).

of the square cross section of the tubes. In all cases, the opening and subsequent propagation of cracks is aligned with the meridional direction and perpendicular to the circumferential direction along which major principal stresses σ_θ are applied. This observation allows concluding that crack opening in tube expansion is by tension (mode I of fracture mechanics).

The finite element estimates of the force versus displacement evolutions in Figure 5(a)–(c) reveal a good agreement up to the peak values. No estimates are provided beyond these values because the finite element models did not account for crack opening and propagation.

Principal strain space

In order to plot the finite element computed strain loading paths in principal strain space and compare against those acquired by DIC, it is first necessary to transform the finite element results from global to local coordinates

by using equation (8). The overall comparison after transformation of coordinates is shown in Figure 6(a)–(c) for tube expansions with circular, elliptical and square cross-section punches. As seen, the good correlation between experimental and numerical force–displacement evolutions of section 'Displacement-based evolutions' also applies for the strain paths in principal strain space.

The finite element computed strain paths are provided for both the inner and outer tube surfaces adjacent to the expanded tube end where necking starts, but only the results of the outer surfaces can be compared against those obtained by DIC.

In general, the finite element computed strain paths are similar for the inner and outer tube surfaces. A minor deviation is found in the expansion with a square cross-section punch at the early stages of deformation during which the strain path of the inner tube surface slightly moves towards pure shear deformation conditions. This is attributed to the very small inner radius
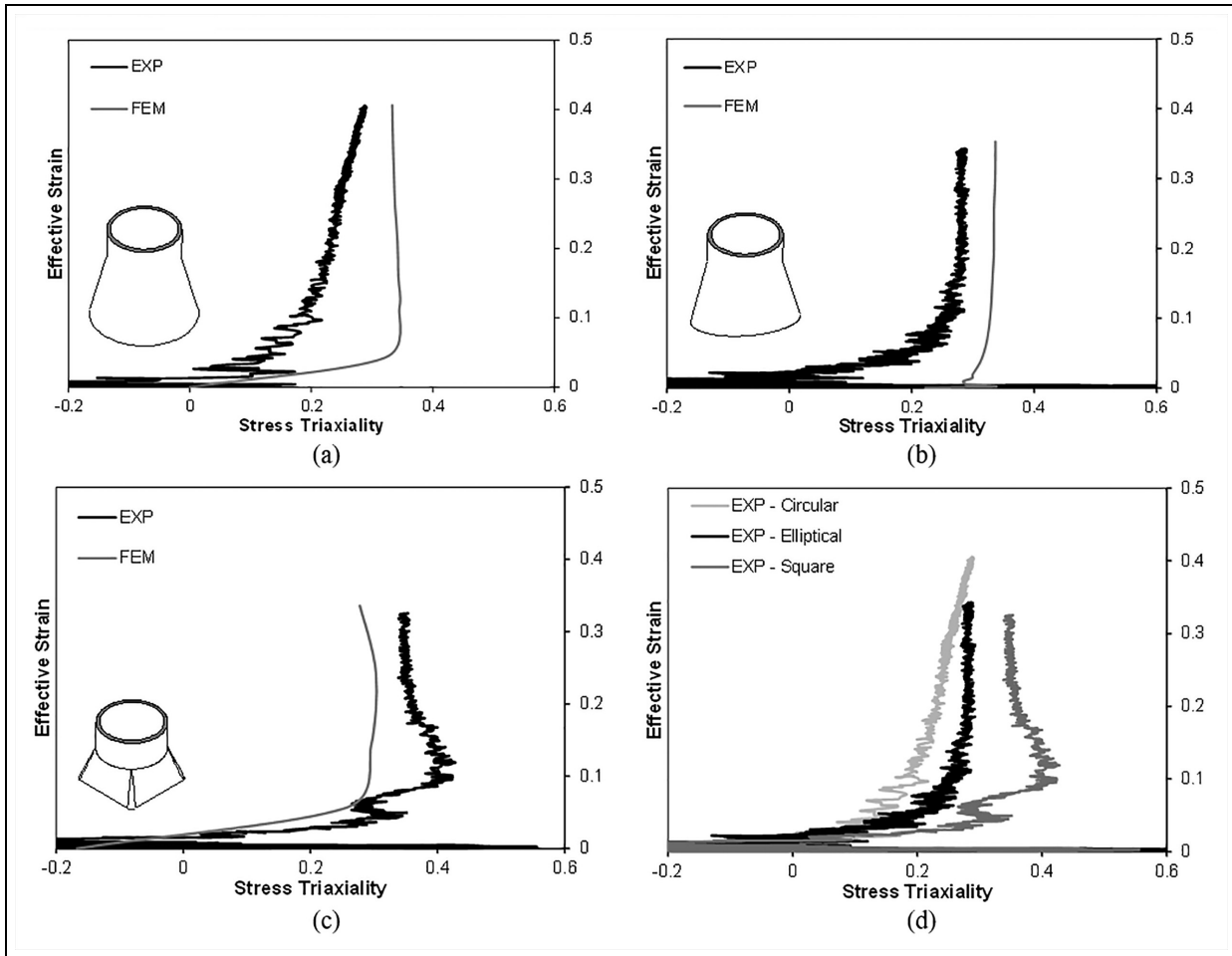
Figure 7. Experimental and finite element computed evolution of the effective strain with stress-triaxiality for the (a) circular, (b) elliptical and (c) square cross-section punches. The resume of the three experimental evolutions in shown in (d).

R_c of the square cross-section punch, which is almost identical to the tube wall thickness.

The last points $(\varepsilon_\theta^n, \varepsilon_\phi^n)$ of the strain loading paths (refer to the black solid lines in Figure 6(a)–(c)) represent the condition of the uniformly thinned tube wall just before necking. In other words, they represent the onset of failure by necking and correspond to the maximum and minimum peak values of the experimental strain–displacement evolutions of Figure 5(a)–(c).

After the onset of necking, the strain paths experience a sharp bend towards the vertical direction corresponding to plane-strain deformation conditions, as it is schematically plotted by the black vertical dashed lines that go up to the fracture strain pairs $(\varepsilon_\theta^f, \varepsilon_\phi^f)$ given by the open markers of Figure 6(a)–(c). The fracture strain pairs were determined from the 'gauge length' strains in accordance to the procedure described in the 'Methodology' section.

Space of effective strain versus stress-triaxiality

The transformation of the experimental strain loading paths from principal strain space to the space of effective strain versus stress-triaxiality was performed in accordance to the procedure described in the 'Methodology' section.

The result of applying equation (3) to the experimental strain loading paths of Figure 6(a)–(c) is shown in Figure 7(a)–(c) (refer to the evolutions labelled as 'EXP'). The other results included in Figure 7(a)–(c) correspond to the finite element estimates of the evolution of the effective strain with stress-triaxiality for the outer surfaces of the tube end.

As seen in Figure 7, the overall agreement between numerical and experimental strain loading paths in the space of effective strain versus stress-triaxiality is fair and the experimental end points in each graphic allow us to identify three different points of the failure locus by necking (Figure 7(d)). Major deviations like those observed at the early stages of tube expansion with a conical punch are attributed to the sensitivity of calculating stress-triaxiality from equation (3) in cases disclosing small differences between the experimental and numerical in-plane strains (refer also to Figure 6(a)).

Another possible reason for the above-mentioned deviation is the friction between the punch and the tube. This is because contact in the circular cross-section punch takes place along the entire interface

Table 2. Critical experimental and numerical values of ductile damage at the onset of failure by necking D_{crit}^n.

Geometry	D_{crit}^n (experimental)	D_{crit}^n (finite element analysis)
Circular	0.09	0.13
Elliptical	0.09	0.11
Square	0.11	0.12
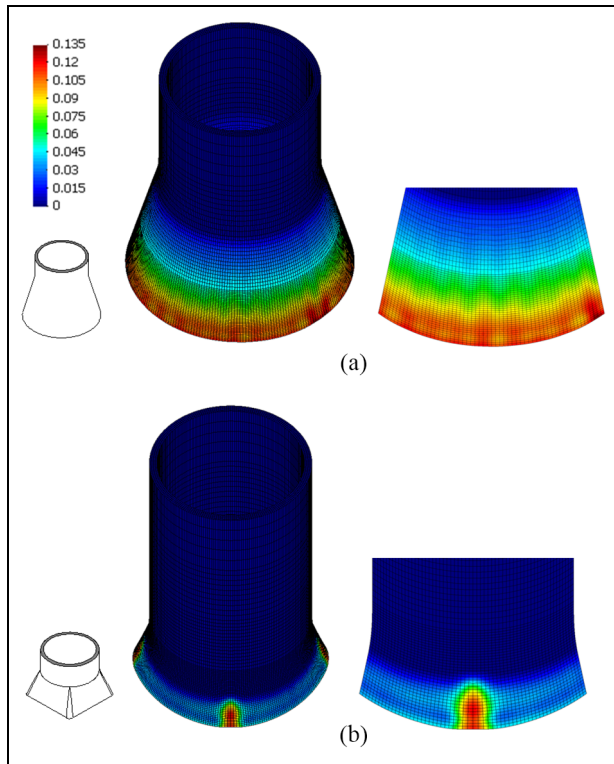
Figure 8. Finite element predicted distribution of accumulated damage according to McClintock stress-triaxiality-based criterion at the onset of failure for tube expansion with (a) conical and (b) square cross-section punches.

whereas contact in the square cross-section punch is mainly localized as a result of tube bending at the punch corners, which moves the tube away from the punch sides. Therefore, instead of using the same friction factor m in all the numerical simulations, better agreement could probably be obtained if the friction factor m was tuned for each punch geometry. However, authors decided not to do that.

Ductile damage at the onset of failure by necking

Once the loading paths are transformed from principal strain space to the space of effective strain versus stress-triaxiality (Figure 7), it is possible to determine the critical experimental value of ductile damage at the onset of failure by necking D_{crit}^n. This is done by calculating the areas that are limited by the experimental loading paths

and the vertical axis (refer to equation (4) and Figure 1(d)).

The results of these calculations are summarized in Table 2 and compared against those obtained from finite element modelling. The values of D_{crit}^n are consistent and major differences between experimental and numerical predictions are found for tube expansion with a circular cross-section punch.

Figure 8 shows the computed distribution of D_{crit}^n for tube expansions with circular and square cross-section punches in which deviations between experimental and numerical predictions are larger and smaller, respectively. Despite the differences observed in Table 2, it is worth noticing that the maximum values of accumulated damage at the onset of failure predicted by finite element analysis are similar and their locations are consistent with the regions of the real tube specimens where necking starts and cracks occur (refer to pictures in Figure (5)).

A possible explanation for the overall differences between experimental and numerical values of ductile damage may be related to the fact that the void-growth damage-based criterion (4) utilized in this investigation is implemented as a non-coupled ductile damage model in the finite element computer programme. This means that nucleation, void growth and void coalescence will influence the experimental values of strains and stresses in the regions where cracks are triggered but will not influence the corresponding finite element estimates, which are slightly higher.

By extending the proposed methodology to other tube forming processes with different strain loading paths, it is possible to obtain the failure locus by necking and fracture and to determine the critical values of ductile damage for other values of stress-triaxiality. This will allow characterizing the formability limits of tube forming for a wider range of stress-triaxiality conditions.

Conclusion

A new methodology to characterize formability in tube forming was successfully applied to tube expansion with circular, elliptical and square cross-section punches. The methodology makes use of DIC, thickness measurements and force–displacement evolutions to obtain the strain loading paths, the strain values at the onsets of failure by necking and fracture and the critical experimental value of ductile damage at the onset of failure by necking.

One of the key innovative features of the proposed methodology is the straightforward identification of the onset of failure by necking from the experimental force and strain–displacement evolutions. This makes the identification of the onset of necking much simpler than in case of sheet forming where interpolation procedures are needed to obtain the experimental strains at the onset of failure by necking.

The onset of fracture was determined by measuring the 'gauge length' strains in the cracked regions of the tubes after testing by means of an experimental technique that extends to tube forming a procedure that has been successfully utilized by the authors in sheet forming.

Combination of the new proposed experimental methodology with finite element analysis allowed authors to check the overall consistency of their experimental measurements and of the critical values of ductile damage at the onset of failure by necking for three different loading paths corresponding to the three different punch geometries. The predicted locations of the maximum accumulated damage are consistent with the experimental observations of necking and subsequent cracking by opening mode I in real tube specimens.

Declaration of conflicting interests

The author(s) declared no potential conflicts of interest with respect to the research, authorship and/or publication of this article.

Funding

ORCID iD

Paulo AF Martins https://orcid.org/0000-0002-2630-4593

References

1. Schreier H, Orteu JJ and Sutton MA. *Image correlation for shape, motion and deformation measurements: basic concepts, theory and applications*. New York: Springer, 2009.
2. Merklein M, Kuppert A and Geiger M. Time dependent determination of forming limit diagrams. *CIRP Ann* 2010; 59: 295–298.
3. Silva MB, Martínez-Donaire AJ, Centeno G, et al. Recent approaches for the determination of forming limits by necking and fracture in sheet metal forming. *Procedia Eng* 2015; 132: 342–349.
4. Tuninetti V, Gilles G, Péron-Lührs V, et al. Compression test for metal characterization using digital image correlation and inverse modeling. *Procedia IUTAM* 2012; 4: 206–214.
5. Magrinho JP, Silva MB, Alves LM, et al. New methodology for the characterization of failure by fracture in bulk forming. *J Strain Anal Eng Des* 2018; 53: 242–247.
6. Dick CP and Korkolis YP. Mechanics and full-field deformation study of the ring hoop tension test. *Int J Solids Struct* 2014; 51: 3042–3057.
7. Ding Y, Kim JS, Kim H, et al. Evaluation of anisotropic deformation behaviours in H-charged Zircaloy-4 tube. *J Nucl Mater* 2018; 508: 440–450.
8. Yang Z, Yan H, Huang C, et al. Experimental and numerical study of circular stainless thin tube energy absorber under axial impact by a control rod. *Thin-Wall Struct* 2014; 82: 24–32.
9. Scales M, Tardif N and Kyriakides S. Ductile failure of aluminium alloy tubes under combined torsion and tension. *Int J Solids Struct* 2016; 97–98: 116–128.
10. McClintock FA. A criterion for ductile fracture by the growth of holes. *J Appl Mech* 1968; 35: 363–371.
11. Cristino VAM, Silva MB, Wong PK, et al. Determining the fracture forming limits in sheet metal forming: a technical note. *J Strain Anal Eng Des* 2017; 52: 467–471.
12. ASTM E8/E8M. Standard test methods for tension testing of metallic materials, 2013.
13. Centeno G, Silva MB, Alves LM, et al. Towards the characterization of fracture in thin-walled tube forming. *Int J Mech Sci* 2016; 119: 12–22.
14. Nielsen CV, Zhang W, Alves LM, et al. *Modeling of thermo-electro-mechanical manufacturing processes with applications in metal forming and resistance welding*. London: Springer-Verlag, 2013.
15. ISO 12004-2:2008. Metallic materials – sheet and strip – determination of forming-limit curves – part 2: determination of forming-limit curves in the laboratory, 2008.